# Beam polarization effects on Z-boson pair production at electron-positron colliders: A full one-loop analysis

Mehmet Demirci<sup>1,2,\*</sup> and A. Baha Balantekin<sup>1,†</sup>

<sup>1</sup>Department of Physics, University of Wisconsin-Madison, Madison, Wisconsin 53706, USA
<sup>2</sup>Department of Physics, Karadeniz Technical University, Trabzon 61080, Turkey



(Received 1 August 2022; accepted 23 September 2022; published 13 October 2022)

We present high-precision predictions for Z boson-pair production via electron-positron collisions by taking into account a full set of one-loop order scattering amplitudes, i.e., electroweak (EW) corrections together with soft and hard QED radiation. We provide a detailed numerical evaluation, from full EW corrections to pure QED corrections, specifically focusing on the effect of initial beam polarization on the production rate. The left-right asymmetry and angular distributions are also presented. The radiative corrections are largely affected by initial beam polarizations. We get an improvement of around three times with completely polarized beams of  $e_L^-$  and  $e_R^+$ . We find that the radiative corrections can sizably modify the production rate, typically yielding a total relative correction up to a few tens of a percent. This implies that the full EW corrections are required for  $e^-e^+ \to ZZ$  to match with percent-level accuracy.

DOI: 10.1103/PhysRevD.106.073003

#### I. INTRODUCTION

The Standard Model (SM) [1–3] has been well established as a self-consistent gauge theory. Starting with the discovery of the Higgs boson [4,5] a decade ago, we have increasing confidence in the consistency of the Standard Model (SM) from the LHC experiments [6]. Despite its many successes, there are remaining questions (such as the hierarchy problem, neutrino masses, dark matter, the strong *CP* problem, and the generation of a baryon asymmetry) which require beyond the SM (BSM) physics. Current and future experiments will continue to not only make sensitivity tests of the SM but also to search for BSM physics to meet the challenges listed above.

Proton-proton colliders have significant backgrounds, which makes it harder to explore rare processes. On the other hand, electron-positron colliders have cleaner backgrounds and offer important opportunities to precisely observe the interesting phenomena. Various proposals for such colliders exist; the International Linear Collider (ILC) [7–9] is one of the proposed linear colliders, which would be operated in the c.m. energies of  $\sqrt{s} = 250-500$  GeV (extendable up to a 1 TeV) with collision modes of  $e^-e^+$ ,  $e^-e^-$ ,  $e^-\gamma$ , and  $\gamma\gamma$ . At the ILC, it is also expected to use the

\*Corresponding author. mehmetdemirci@ktu.edu.tr †baha@physics.wisc.edu

Published by the American Physical Society under the terms of the Creative Commons Attribution 4.0 International license. Further distribution of this work must maintain attribution to the author(s) and the published article's title, journal citation, and DOI. Funded by SCOAP<sup>3</sup>. electron and positron beams with 80% and 30% polarizations, respectively. Another linear collider is the Compact Linear Collider (CLIC) [10], which is foreseen to be operated a TeV scale high-luminosity capacity, in stages at energies of  $\sqrt{s} = 380$  GeV, 1.5 TeV, and 3 TeV,. Furthermore, there are circular collider projects such as the Circular Electron-Positron Collider (CEPC) [11] and Future Circular Collider (FCC) [12]. The CEPC is projected with a circumference of 100 km and to have a maximum of  $\sqrt{s} = 240 \text{ GeV}$ . The FCC project [12], hosted in a 100 km tunnel at CERN, is considering three collision types: FCC-ee, for electron-positron collisions; FCC-hh, for hadron-hadron collisions; and FCC-eh, for electron-hadron collisions. The FCC-ee [13], running at different energies to research the production of Z, W, H and  $t\bar{t}$ , is expected to be a Higgs, electroweak, and top factory with high luminosity. The above lepton colliders are expected to offer the unique opportunities for precise measurements and signs of new physics, appearing in the form of small deviations from the SM.

In parallel, high-precision predictions from theory are required to get more precise measurements for clues of the BSM physics or more sensitivity tests of the SM. This means that it is necessary to go beyond the lowest-order calculations for the most production channels. At least, one-loop order corrections in the production channels must be included to get adequate accuracy. However, the extent to which higher-order computations beyond one-loop order will be needed depends largely on the expected experimental accuracy. In the present study, we focus on the complete one-loop-order electroweak (EW) corrections and beam polarization effects. The beam polarization has the

ability to improve the corresponding signal-to-background ratio along with the sensitivity of the observables [14–16]. Furthermore, the *CP*-violating couplings can be separated from *CP*-conserving ones using beam polarization [16].

The main production reaction of the Z-boson pairs at the  $e^-e^+$  colliders are  $e^-e^+ \to ZZ$ , which include the Bornlevel contributions from electron exchanges via t and u- channels. Since there are no Yukawa or QCD contributions, the identification of the EW corrections would be very clean. The process at Born order was studied by Refs. [17,18] a long time ago. Next, one-loop EW radiative corrections were investigated by Ref. [19]. However, their results directly depend on the soft cutoff parameter, since the hard photon correction is not taken into account. In addition to the above work, in Ref. [20], the high-energy behavior of the various helicity amplitudes was investigated considering all of the Minimal Supersymmetric Standard Model contributions.

Furthermore, neutral gauge boson production via electron-positron collisions have received a significant experimental [21–23] and theoretical [24–28] interest, motivated by the search for anomalous neutral gauge boson self-couplings. In particular, *Z*-pair events provide an opportunity for the investigation of possible triple neutral gauge boson couplings,  $ZZ\gamma$  and ZZZ [29–31], not allowed at tree level in the SM.

In the present work, we examine the Z-boson pair production via electron-positron collisions in the SM, including a full set of one-loop-order EW radiative corrections, i.e., the EW corrections together with soft and hard real photon emission. We provide a detailed numerical discussion with particular emphasis on the effects of initial beam polarization. Moreover, we consider the decomposition of the EW corrections into the pure QED photonic corrections along with the corresponding counterterms and the remaining weak corrections. The left-right asymmetry and angular distributions are also presented at the Born and one-loop orders.

The rest of this paper is organized as follows. In Sec. II, we provide some useful analytical expressions together with the relevant Feynman diagrams and amplitudes. General shapes of the real photon emission and the virtual corrections are also discussed. In Sec. III, we give briefly information on initial beam polarization. In Sec. IV, we give a set of input parameters used in this study. In Sec. V, we present a detailed analysis of numerical results. A comparison with the results of other approaches is also given. Finally, in Sec. VI, we present a summary and conclusions.

# II. THEORETICAL SETUP FOR A CROSS SECTION

We first present our notation regarding the Born amplitudes and one-loop EW contributions. The relevant production process is expressed as

$$e^+(p_1, \sigma_1)e^-(p_2, \sigma_2) \to Z(k_1, \lambda_1)Z(k_2, \lambda_2),$$
 (2.1)

where  $\sigma_1$ ,  $\sigma_2$ ,  $\lambda_1$ , and  $\lambda_2$  denote the helicities of initial positron and electron and outgoing Z bosons, respectively. The helicities take the values  $\lambda_{1,2}=0,\pm 1$  and  $\sigma_{1,2}=\pm 1/2$ . Polarization vectors of outgoing Z bosons are denoted by  $\varepsilon_\mu(k_1,\lambda_1)$  and  $\varepsilon_\nu(k_2,\lambda_2)$ . Neglecting the electron mass, the momenta in the center of mass of the initial state system are given by

$$p_{1} = \frac{\sqrt{s}}{2}(1, 0, 0, -1),$$

$$p_{2} = \frac{\sqrt{s}}{2}(1, 0, 0, +1),$$

$$k_{1} = \frac{\sqrt{s}}{2}(1, -\kappa \sin \theta, 0, -\kappa \cos \theta),$$

$$k_{2} = \frac{\sqrt{s}}{2}(1, +\kappa \sin \theta, 0, +\kappa \cos \theta),$$
(2.2)

where

$$\kappa = \sqrt{1 - \frac{4M_Z^2}{s}},\tag{2.3}$$

and  $\sqrt{s}$  and  $\theta$  denotes the center-of-mass energy and the scattering angle, respectively. For further use, we also note the Mandelstam variables:

$$s = (p_1 + p_2)^2 = (k_1 + k_2)^2,$$
  

$$t = (k_1 - p_1)^2 = (k_2 - p_2)^2,$$
  

$$u = (k_2 - p_1)^2 = (k_1 - p_2)^2.$$
 (2.4)

The Z-boson polarization vectors are given by

$$\varepsilon_{+}^{\mu}(k,\lambda=+1) = -\frac{1}{\sqrt{2}}(0,1,i,0), 
\varepsilon_{0}^{\mu}(k,\lambda=0) = \frac{1}{M_{Z}}(k_{z},0,0,E), 
\varepsilon_{-}^{\mu}(k,\lambda=-1) = \frac{1}{\sqrt{2}}(0,1,-i,0),$$
(2.5)

which obey the condition  $\varepsilon^{\mu}k_{\mu} = 0$ . The sum over physical polarization states of the Z boson is given by

$$\sum_{\lambda} \varepsilon_{\mu}(k,\lambda) \varepsilon_{\nu}^{*}(k,\lambda) = -g_{\mu\nu} + \frac{k_{\mu}k_{\nu}}{M_{Z}^{2}}.$$
 (2.6)

The analytical and numerical evaluations are carried out by using the following tools. The Feynman diagrams and

<sup>&</sup>lt;sup>1</sup>Using the same tools, many calculations have been carried out with significant results (see, e.g., Refs. [32–35] by one of us and Refs. [36–40] by others).

amplitudes are created by using FEYNARTS [41,42]. The algebraic evaluation for amplitudes is provided technically in the same way as defined in Ref. [35]. Then, the squaring of amplitudes, the simplifying of fermion chains and the numerical computation are carried out by using FORMCALC [43]. The scalar loop integrals are calculated via LOOPTOOLS [43]. The phase-space integrations are calculated by using the Monte Carlo integration algorithm VEGAS, implemented in the CUBA library [44]. We have checked the cross sections of Born and hard photon radiation processes against the results obtained by using WHIZARD [45,46] and CALCHEP [47].

## A. Born amplitudes

At lowest order, the process  $e^+e^- \to ZZ$  includes the leading contributions from t- and u-channel electron-exchange diagrams. The corresponding Feynman diagrams are given in Fig. 1, where a diagram with a Higgs field coupling to electrons is omitted. It is suppressed by a factor  $m_e/\sqrt{s}$  and thus can be neglected. The explicit expressions are given for the Born matrix elements from these diagrams as

$$\begin{split} \mathcal{M}_{1} &= \frac{-ig^{2}}{4[t - m_{e}^{2}]c_{W}^{2}} \bar{v}(p_{1}, m_{e}) \mathscr{E}^{*}(k_{1})[c_{V}^{e} - c_{A}^{e}\gamma_{5}] \\ &\times (\mathscr{P}_{2} - \mathscr{U}_{2} + m_{e}) \mathscr{E}^{*}(k_{2})[c_{V}^{e} - c_{A}^{e}\gamma_{5}] u(p_{2}, m_{e}), \end{split} \tag{2.7}$$

$$\mathcal{M}_{2} = \frac{-ig^{2}}{4[u - m_{e}^{2}]c_{W}^{2}} \bar{v}(p_{1}, m_{e}) \mathscr{E}^{*}(k_{2})[c_{V}^{e} - c_{A}^{e}\gamma_{5}]$$

$$\times (\cancel{p}_{2} - \cancel{k}_{1} + m_{e}) \mathscr{E}^{*}(k_{1})[c_{V}^{e} - c_{A}^{e}\gamma_{5}] u(p_{2}, m_{e}),$$

$$(2.8)$$

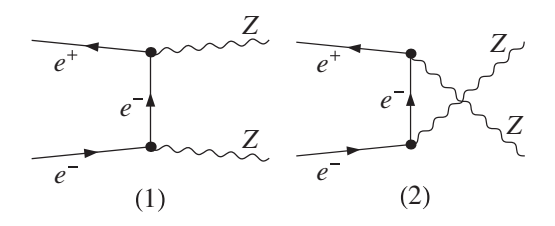


FIG. 1. The lowest-order Feynman diagrams contributing to  $e^-e^+ \rightarrow ZZ$ .

where  $g=e/s_W$ ,  $s_W=\sin\theta_W$ , and  $c_W=\cos\theta_W=M_W/M_Z$ . The vector and axial vector couplings are defined as  $c_V^f=I_3^f-2Q_fs_W^2$  and  $c_A^f=I_3^f$  for the fermion type f. For electrons, these are  $c_V^e=-1/2+2s_W^2$  and  $c_A^e=-1/2$ . The Born-level total amplitude is

$$\mathcal{M}_{\text{Bom}} = \sum_{i=1}^{2} \mathcal{M}_{i}.$$
 (2.9)

For arbitrary polarizations of the leptons and bosons, the differential cross section reads

$$\left(\frac{d\sigma}{d\Omega}\right)_{\text{Bom}}^{e^{+}e^{-}\to ZZ} = \frac{\kappa}{64\pi^{2}s} \sum_{\sigma_{1,2},\lambda_{1,2}} \frac{1}{4} (1 + 2\sigma_{1}P_{1})(1 + 2\sigma_{2}P_{2}) \times |\mathcal{M}_{\text{Bom}}^{\sigma_{1},\sigma_{2},\lambda_{1},\lambda_{2}}|^{2}, \tag{2.10}$$

where  $P_1$  and  $P_2$  are the polarization degrees of the incoming electron and positron. The sum runs over all included boson polarizations. Following the square of total amplitude and the summation over final helicities, we have

$$\left(\frac{d\sigma}{dt}\right)_{\text{Bom}}^{e^-e^+\to ZZ} = \frac{g^4}{128\pi^2 s^2} \frac{(c_V^e)^4 + (c_A^e)^4 + 6(c_V^e)^2(c_A^e)^2}{c_W^4} \left[\frac{u}{t} + \frac{t}{u} + 4M_Z^2\left(\frac{s}{ut}\right) - M_Z^4\left(\frac{1}{t^2} + \frac{1}{u^2}\right)\right], \tag{2.11}$$

where the electron mass  $m_e$  is neglected for simplicity. This result is consistent with the results in the literature [17]. The above coupling term can be also written in terms of chiral coupling constants as  $(c_V^e)^4 + (c_A^e)^4 + 6(c_V^e)^2(c_A^e)^2 = 8(c_L^e)^4 + 8(c_R^e)^4$ . Then, the integrated cross section is obtained by

$$\sigma_{\text{Born}}^{e^-e^+ \to ZZ} = \frac{1}{2!} \int_{t_{\text{min}}}^{t_{\text{max}}} \left( \frac{d\sigma}{dt} \right)_{\text{Born}}^{e^-e^+ \to ZZ} dt, \qquad (2.12)$$

where the lower and upper bounds of the integral are defined as

$$t_{\text{max,min}} = M_Z^2 - \frac{1}{2}s(1 \pm \kappa).$$
 (2.13)

# B. One-loop EW radiative corrections

The radiative corrections consist of three parts. The first comes from virtual loop corrections, the second one is soft photon radiation, and the last one corresponds to hard real photon radiation. We now discuss them for  $e^-e^+ \rightarrow ZZ$  below.

## 1. Virtual corrections

We consider full EW  $\mathcal{O}(\alpha)$  contributions at one-loop level for the process  $e^-e^+ \to ZZ$ . The virtual loop corrections for this process come from three types of diagrams: vertex type, self-energy, and box type. Here, we do not provide their explicit analytical expressions since they are not particularly illuminating. Instead, we present a

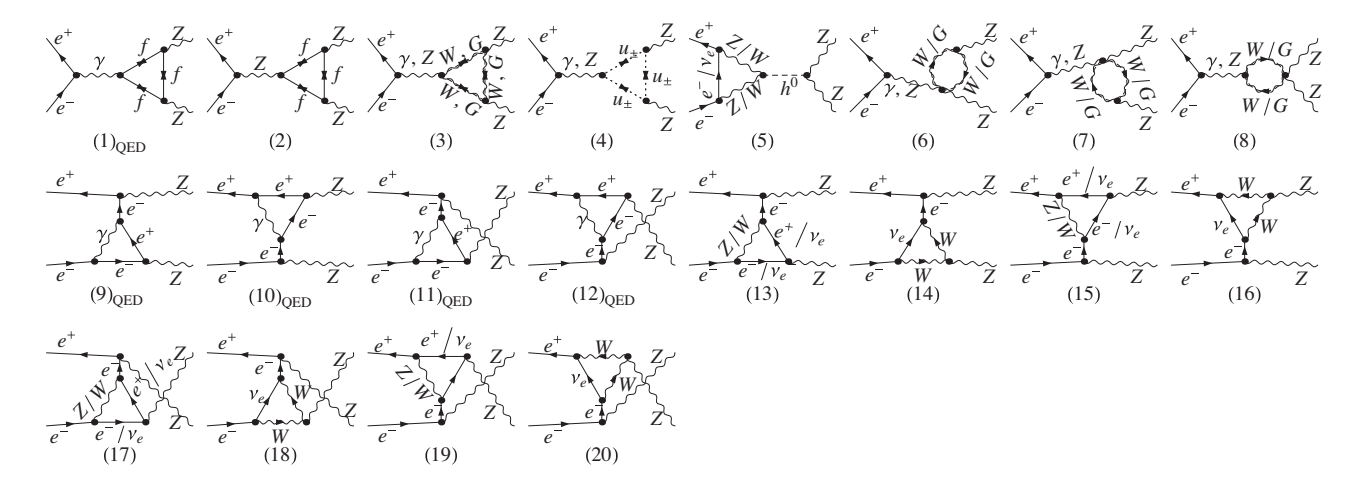


FIG. 2. The vertex-correction diagrams contributing to  $e^-e^+ \rightarrow ZZ$ .

complete list of Feynman diagrams created by FEYNARTS. At one-loop order, the process (2.1) has a total of 161 one-loop diagrams (112 vertextype + 34 self-energy + 15 boxtype) as shown in Figs. 2–4. We use the following labels on the internal lines: f stands for all fermions in SM, G is the charged Goldstone boson, and  $u_{\pm}$  is the ghosts. The gauge vector bosons ( $\gamma$ , Z, and  $W^{\pm}$ ) are denoted by wavy lines, and the Higgs and Goldstone bosons are denoted by the dashed lines. In diagrams with two arrows on the same lines of the loop, particles move both clockwise and counterclockwise.

The one-loop diagrams can topologically divided into s, t, and u channels with the mediator of gauge bosons ( $\gamma$ , Z,  $W^{\pm}$ ), Higgs boson ( $h^0$ ), and charged Goldstone bosons ( $G^{\pm}$ ). We can also separate them into QED and weak corrections. The diagrams of QED virtual corrections are obtained by the possible virtual photon attachment and fermion loop insertion to the Born-level diagrams.

First, in Fig. 2, we present the vertex-correction diagrams, which consist of triangle corrections to *t*-channel

electron exchange, bubbles, and triangle vertices attached to the initial or final state via a mediator of  $\gamma$ , Z, and  $h^0$ . They can also be divided into three classes. The first comes from the vertex corrections  $ZZA^*/Z^*$ . Here, the offshell field is marked by an asterisk. These are given with diagrams 1–4 and 6–8 in Fig. 2. The second is due to the vertex corrections  $eeh^{0*}$ , and it is shown in diagram 5 in Fig. 2. Both types are s-channel contributions. The fermion loop contributions to the vertex of  $eeh^{0*}$  are proportional to the electron mass and hence are suppressed. The third type is the vertex corrections  $Ze\bar{e}^*$  in the t and u channels. The  $Ze\bar{e}^*$  correction is shown in diagrams 9–20 of Fig. 2.

Second, in Fig. 3, we show the self-energy diagrams, which consist of all possible loops of  $e^-$  or  $\nu_{e^-}$  with gauge bosons  $\gamma$ , Z, or  $W^\pm$  on the electron propagator via t and u channels. Also, all possible loops of fermions, W and G bosons are included on the  $\gamma h^0$  or  $Zh^0$  mixing propagator in s channel. Diagrams 4 and 5 in Fig. 3 are obtained by QED correction, while others are weak corrections.

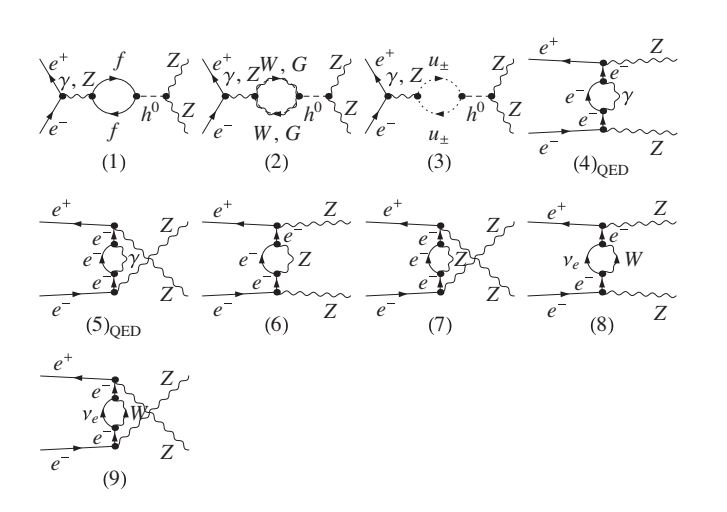


FIG. 3. The self-energy diagrams contributing to  $e^-e^+ \rightarrow ZZ$ .

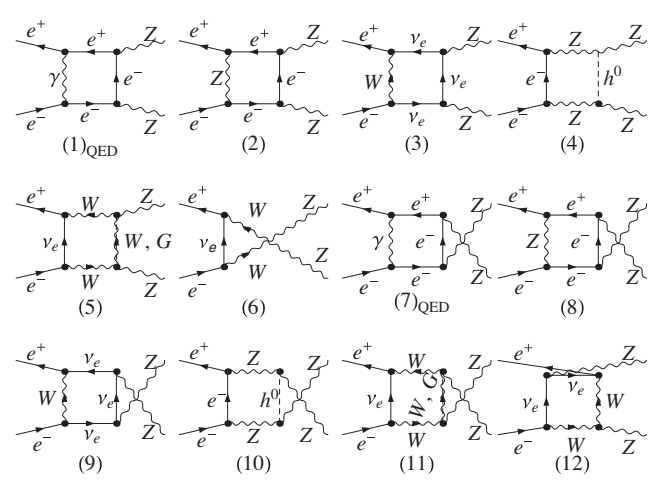


FIG. 4. The box-type diagrams contributing to  $e^-e^+ \rightarrow ZZ$ .

Finally, Fig. 4 shows the irreducible one-loop diagrams (box-type diagrams). They consist of all possible box loops of  $e^-$ ,  $\nu_{e^-}$ , vector bosons  $\gamma$ , Z,  $W^\pm$ , Higgs and Goldstone bosons. These are mainly  $t^-$  and u-channel contributions. Diagrams 1 and 7 in Fig. 4 are obtained by QED correction, while others are weak corrections. Diagrams 2, 4, 8, and 10 are due to neutral current correction, and other diagrams are due to charged current correction.

The total amplitude for the virtual contributions is defined as the summation of triangle-type, self-energy, and box-type corrections:

$$\delta M_{\text{virt}} = \mathcal{M}_{\wedge} + \mathcal{M}_{\bigcirc} + \mathcal{M}_{\square}. \tag{2.14}$$

The differential cross section of the virtual corrections is calculated by

$$\left(\frac{d\sigma}{d\Omega}\right)_{\text{virt}}^{e^-e^+ \to ZZ} = \sum_{\sigma_{1,2}, \lambda_{1,2}} \frac{1}{4} (1 + 2\sigma_1 P_1) (1 + 2\sigma_2 P_2) 
\times \frac{\kappa}{64\pi^2 s} 2 \text{Re}[\mathcal{M}_{\text{Born}}^* \delta M_{\text{virt}}],$$
(2.15)

where  $|\delta M_{\rm virt}|^2$  is not included because its contribution is so small that it can be neglected. The one-loop Feynman diagrams, which form the virtual  $\mathcal{O}(\alpha)$  corrections  $\delta M_{\rm virt}$ , have been calculated in the 't Hooft-Feynman gauge. We use the on-shell (OS) renormalization scheme (see Ref. [48]) to fix all the renormalization constants.

The virtual contributions have UV and IR divergences. These divergences can be regularized by extending the dimensions of spinor and spacetime manifolds to D = $4-2\epsilon$  [49] and adding a photon mass parameter, respectively. We adopt all Feynman rules of the counterterms (shown in Fig. 5) and of the renormalization conditions from Ref. [48]. The redefinition of parameters and fields is carried out in the OS scheme. This turns the Lagrangian into a bare term and a counter-term. After applying the renormalization procedure, a UV-finite virtual contribution is achieved. Although, the soft IR singularity due to virtual photonic loop corrections still exists. It is regularized by giving the photon a fictitious mass,  $m_{\gamma}$ . The virtual cross section is independent of the UV regularization parameter  $C_{\text{UV}} = 1/\epsilon - \gamma_E + \log(4\pi)$ but still a function of the IR regularization parameter  $m_{\gamma}$ . From the Kinoshita-Lee-Nauenberg theorem [50,51],<sup>2</sup> it is canceled in the limit  $m_{\gamma} \rightarrow 0$  by adding the real photon corrections. We have checked numerically that our results do not depend on  $m_{\gamma}$ . After adding the virtual and real corrections, the results are still collinear singular. This singularity comes from the initial-state radiation part. We use the phase-space slicing method<sup>3</sup> [53–56] to

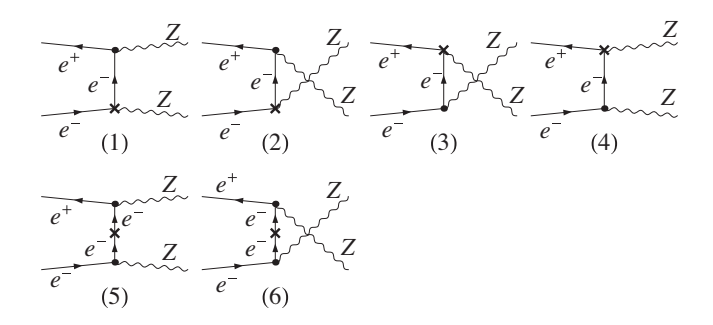


FIG. 5. The counterterm diagrams.

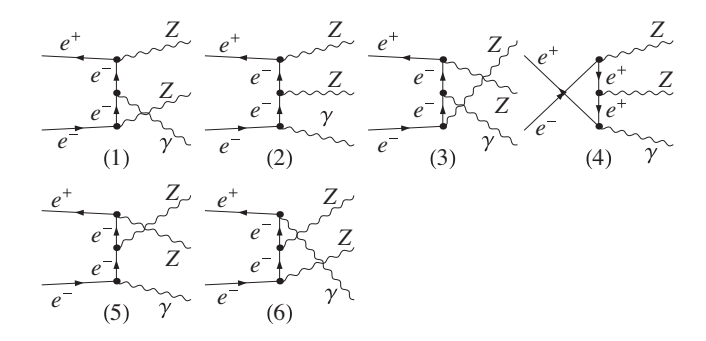


FIG. 6. The Feynman diagrams for the real photon radiation.

handle the collinear singularities in the photon radiation off the initial state.

#### 2. Real corrections

Real photon emission gives rise to the kinematically different reaction from  $e^+e^- \rightarrow ZZ$ , presented by

$$e^{+}(p_1, \sigma_1)e^{-}(p_2, \sigma_2) \rightarrow Z(k_1, \lambda_1)Z(k_2, \lambda_2)\gamma(k_3, \lambda_3),$$
(2.16)

where  $k_3$  and  $\lambda_3$  are the 4-momenta and helicity of the radiated photon. We present the bremsstrahlung Feynman diagrams in Fig. 6, obtained from the Born diagrams by adding a photon emitted from a lepton line. The lowest-order of real-photon emission provides an  $\mathcal{O}(\alpha)$  correction to  $e^+e^- \to ZZ$ .

The differential cross section of  $e^+e^- \rightarrow ZZ\gamma$  reads

$$\left(\frac{d\sigma}{d\Omega_{3}}\right)_{\text{real}}^{e^{+}e^{-}\to ZZ\gamma} = \frac{1}{2s} \sum_{\sigma_{1,2},\lambda_{1,2,3}} \frac{1}{4} (1 + 2P_{1}\sigma_{1})(1 + 2P_{2}\sigma_{2}) 
\times |\mathcal{M}_{e^{+}e^{-}\to ZZ\gamma}^{\sigma_{1},\sigma_{2},\lambda_{1},\lambda_{2},\lambda_{3}}|^{2}$$
(2.17)

with the three-particle phase-space integral

<sup>&</sup>lt;sup>2</sup>This was also shown perturbatively in QED by Schwinger [52].

<sup>&</sup>lt;sup>3</sup>We have developed the necessary code for evaluating of collinear contributions and implemented it in FORMCALC.

$$\int d\Omega_3 = \prod_{i=1}^3 \int \frac{d^3 \vec{k}_i}{(2\pi)^3 2k_i^0} (2\pi)^4 \delta\left(p_1 + p_2 - \sum_{j=1}^3 k_j\right). \tag{2.18}$$

According to the radiated photon energy  $E_{\gamma} = \sqrt{|\vec{k_3}|^2 + m_{\gamma}^2}$ , the bremsstrahlung phase space can be separated into two regions: soft and hard. Hence, the real photon radiation correction can be organized as

$$d\sigma_{\rm real}^{e^-e^+ \to ZZ\gamma} = d\sigma_{\rm soft}(\Delta_s) + d\sigma_{\rm hard}(\Delta_s), \quad (2.19)$$

where  $\Delta_s = \Delta E_\gamma/(\sqrt{s}/2)$  is the soft cutoff energy parameter. The bremsstrahlung photon is named soft when  $E_\gamma < \Delta E_\gamma = \Delta_s \sqrt{s}/2$ , whereas it is hard if  $E_\gamma > \Delta E_\gamma$ . The soft photon correction is given by approximation [48,57],

$$d\sigma_{\text{soft}} = -d\sigma_{\text{Born}} \frac{\alpha Q_{\ell}^2}{2\pi^2} \int_{|\overrightarrow{k_3}| \le \Delta E_{\gamma}} \frac{d^3 k_3}{2E_{\gamma}} \left[ \frac{k_1}{k_1 \cdot k_3} - \frac{k_2}{k_2 \cdot k_3} \right]^2,$$
(2.20)

where  $\Delta E_{\gamma}$  satisfies  $E_{\gamma} \leq \Delta E_{\gamma} \ll \sqrt{s}$ . Integrating the soft photon phase space in the center-of-mass system gives

$$d\sigma_{\text{soft}} = \delta_{\text{soft}} d\sigma_{\text{Born}} \tag{2.21}$$

with

$$\begin{split} \delta_{\rm soft} &= -\frac{\alpha}{\pi} \left[ 2 \ln \left( \frac{2\Delta E_{\gamma}}{m_{\gamma}} \right) \left( 1 + \ln \left( \frac{m_e^2}{s} \right) \right) \right. \\ &\left. + \frac{1}{2} \ln^2 \left( \frac{m_e^2}{s} \right) + \ln \left( \frac{m_e^2}{s} \right) + \frac{\pi^2}{3} \right]. \end{split} \tag{2.22}$$

Both the soft and hard photon corrections depend on the soft cutoff parameter  $\Delta_s$ , but the real correction is independent of this parameter. We note that the hard photon emission must be taken account into to remove this dependency. Furthermore, adding the virtual and soft corrections removes the  $m_{\gamma}$  dependency.

In addition to the divergences mentioned above, there also appear mass singularities as a consequence of the collinear photon emission off massless particles, so-called collinear divergences. However, the smallness of the electron mass induces the quasicollinear IR divergences from the photon radiation off the electron/positron. To deal with this, we apply the phase-space slicing method. According to this method, the hard bremsstrahlung phase space can be divided into collinear and finite regions,

$$d\sigma_{\text{hard}}^{e^-e^+ \to ZZ\gamma}(\Delta_s) = d\sigma_{\text{coll}}(\Delta_s, \Delta_c) + d\sigma_{\text{fin}}(\Delta_s, \Delta_c), \quad (2.23)$$

where  $\Delta_c$  denotes the angular cutoff parameter. In the hard collinear region  $(E_{\gamma} \geq \Delta E_{\gamma}, \cos \theta_{e\gamma} > 1 - \Delta_c)$ , the

integrand is numerically unstable, whereas in the hard finite region  $(E_{\gamma} \ge \Delta E_{\gamma}, \cos \theta_{e\gamma} \le 1 - \Delta_c)$ , it is finite (numerically stable). Here,  $\cos \theta_{e\gamma}$  is the cosines of angle between the electron/positron and bremsstrahlung photon. In the stable regions, the integration is carried out numerically, while it is semianalytically calculated in the unstable regions [58] by using the approximation

$$d\sigma_{\text{coll}} = \sum_{i=1}^{2} \frac{\alpha}{2\pi} Q_i^2 \int_0^{1-\Delta_s} dx \, d\sigma_{\text{Born}}(\sqrt{xs})$$
$$\times \left[ \frac{1+x^2}{1-x} \ln\left(\frac{s\Delta_c}{2m_i^2}\right) - \frac{2x}{1-x} \right], \tag{2.24}$$

where the approximation  $\Delta_c \gg 2m_e^2/s$  has been taken. To avoid overcounting in the soft energy region, the integration over all possible factors x is constrained by the soft cutoff parameter  $\Delta_s$ .

## 3. Classification of full corrections

As a result, the IR- and UV-finite EW corrections consist of four parts,

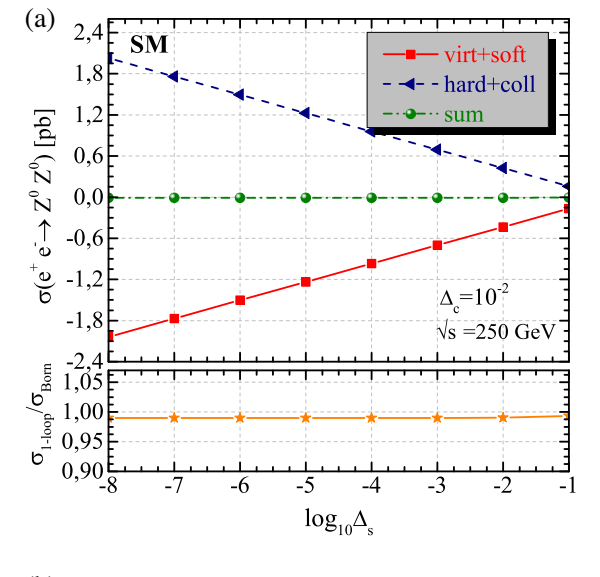
$$d\sigma_{\rm NLO}^{e^+e^- \to ZZ} = d\sigma_{\rm virt}(m_{\gamma}) + d\sigma_{\rm soft}(m_{\gamma}, \Delta_s) + d\sigma_{\rm coll}(\Delta_s, \Delta_c) + d\sigma_{\rm fin}(\Delta_s, \Delta_c), \quad (2.25)$$

where they are from virtual corrections, soft photon corrections, collinear corrections, and finite hard photon corrections, respectively.

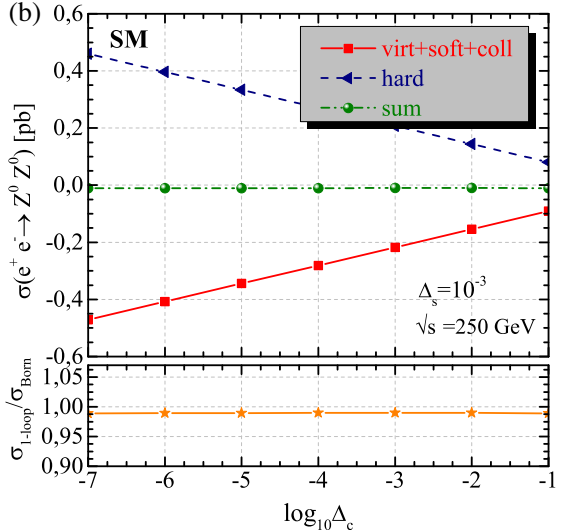
We have numerically checked that our results are independent of  $m_{\gamma}$ , soft cutoff parameter  $\Delta_s$ , and angular cutoff parameter  $\Delta_c$ . The virtual, soft photon, and hard photon emission corrections are shown as a function of both  $\Delta_s$  and  $\Delta_c$  at  $\sqrt{s} = 250$  GeV in Fig. 7. It is obvious that the virtual plus soft and the hard photon emission corrections significantly depend on  $\Delta_s$  and  $\Delta_c$ , whereas the total corrections do not depend on them. Moreover, the relative correction  $\sigma_{1\text{-loop}}/\sigma_{\text{Born}}$  is independent of  $\Delta_s$  and  $\Delta_c$ over several orders of magnitude. To more clearly show the cutoff independence, we have also given the values by tables next to Fig. 7. Finally, our results are also stable over nine digits when varying  $m_{\gamma}$  from  $10^{-20}$  GeV to the default value of 1 GeV. Our numerical results below have been obtained for  $\Delta_s = 10^{-3}$ ,  $\Delta_c = 10^{-2}$ , and the range of scattering angles of the final particles  $|\cos \theta| < 0.99$ .

To discuss the origin of the large correction, we also consider the pure QED corrections  $\delta_{\text{QED}}$  as individual in addition to the full EW corrections  $\delta_{\text{Total}}$ . The QED corrections consist of virtual-photon exchange, the corresponding counterterms, and real-photon emission. Hence, we can express the QED relative correction as

$$\delta_{\text{OED}} = \delta_{\text{virt,OED}} + \delta_{\text{real}}.$$
 (2.26)



$\Delta_s$	$\sigma_{1\text{-loop}}/\sigma_{\mathrm{Born}}$
$10^{-1}$	0.9933
$10^{-2}$	0.9904
$10^{-3}$	0.9899
$10^{-4}$	0.9899
$10^{-5}$	0.9899
$10^{-6}$	0.9898
$10^{-7}$	0.9897
$10^{-8}$	0.9897



$\Delta_c$	$\sigma_{1 ext{-loop}}/\sigma_{\mathrm{Born}}$
$10^{-1}$	0.9891
$10^{-2}$	0.9899
$10^{-3}$	0.9899
$10^{-4}$	0.9897
$10^{-5}$	0.9894
$10^{-6}$	0.9892
$10^{-7}$	0.9889

FIG. 7. Phase-space slicing method. The virtual, soft, and hard photon radiation corrections as a function of soft cutoff parameter  $\Delta_s$  (upper plot) and angular cutoff parameter  $\Delta_c$  (lower plot) at  $\sqrt{s} = 250$  GeV.

The QED-like diagrams consist of only A and f fields as virtual lines. In this study, the one-loop QED contributions come from the sum of the real-photonic corrections and contributions of diagrams 4 and 5 of Fig. 3, 1 and 7 of Fig. 4, and 1 and 9–12 of Fig. 2.

The remaining corrections (non-QED) can be called *weak* corrections  $\delta_{\text{Weak}}$ , which include the massive gauge bosons  $Z^0$  and  $W^{\pm}$ . The genuine weak relative correction can be obtained from

$$\delta_{\text{Weak}} = \delta_{\text{Total}} - \delta_{\text{OED}}.$$
 (2.27)

In the above definition of  $\delta_{Weak}$ , the weak corrections are obtained by subtracting the pure QED corrections from the full EW radiative corrections. Thus, we can write the full  $\mathcal{O}(\alpha)$  EW relative correction as

$$\delta_{\text{Total}} = \delta_{\text{OFD}} + \delta_{\text{Weak}}.$$
 (2.28)

Overall, we can factorize the full EW corrected cross section into the Born cross section and the relative corrections. Therefore, the one-loop cross section  $\sigma_{\text{1-loop}}$  becomes

$$\sigma_{1\text{-loop}} = \sigma_{\text{Born}} (1 + \delta_{\text{Total}})$$

$$= \sigma_{\text{Born}} (1 + \delta_{\text{OFD}} + \delta_{\text{Weak}}), \qquad (2.29)$$

leading to

$$\delta_{\rm X} = \frac{\sigma_{\rm 1-loop}^{\rm X} - \sigma_{\rm Born}}{\sigma_{\rm Born}} \tag{2.30}$$

where X can be "QED," "weak," and "total."

#### III. BEAM POLARIZATION

Polarization effects are important in  $e^+e^-$  colliders and can be used to provide significant advantages. These effects could benefit searches for new physics with small deviation from the SM predictions in two ways. First, properly chosen combinations of beam polarization can strengthen the signal and suppress the background in many cases. Second, it is possible to establish smart observables that contain beam polarization information. With the above motives, we analyze the effect of beam polarizations on the production rate of  $e^+e^- \rightarrow ZZ$ .

The polarizations with a sign for  $e^-$  and  $e^+$  beams are given by [59], respectively,

$$P_{e^{-}} = \frac{(n_{e_{R}^{-}} - n_{e_{L}^{-}})}{(n_{e_{R}^{-}} + n_{e_{L}^{-}})}, \qquad P_{e^{+}} = \frac{(n_{e_{R}^{+}} - n_{e_{L}^{+}})}{(n_{e_{R}^{+}} + n_{e_{L}^{+}})}, \qquad (3.1)$$

where  $n_{e_L^\pm}$  and  $n_{e_R^\pm}$  are the number of the left- and right-handed  $e^\pm$ 's  $(e_L^\pm)$  and  $e_R^\pm$  in the beam, respectively. Here,  $P_{e^-}/P_{e^+}$  is equal to +1 (-1) for the 100% right-handed (left-handed) polarized  $e^-/e^+$  beams.

If a normalization  $n_{e_L^{\pm}} + n_{e_R^{\pm}} = 1$  is applied, the normalized number of  $e_R^-$ 's and  $e_L^-$ 's can be obtained as

$$n_{e_{R}^{-}} = \frac{1 + P_{e^{-}}}{2}, \qquad n_{e_{L}^{-}} = \frac{1 - P_{e^{-}}}{2}.$$
 (3.2)

Consequently, the cross section for any beam polarizations can be defined by [16,59,60]

$$\begin{split} \sigma^{P_{e^{+}}P_{e^{-}}} &= \frac{1}{4} \left[ (1 - P_{e^{+}})(1 - P_{e^{-}}) \sigma_{LL} \right. \\ &+ (1 + P_{e^{+}})(1 + P_{e^{-}}) \sigma_{RR} \\ &+ (1 - P_{e^{+}})(1 + P_{e^{-}}) \sigma_{LR} \\ &+ (1 + P_{e^{+}})(1 - P_{e^{-}}) \sigma_{RL} \right], \end{split} \tag{3.3}$$

where  $\sigma_{LL}$ ,  $\sigma_{RR}$ ,  $\sigma_{LR}$ , and  $\sigma_{RL}$  indicate the cross sections with completely polarized beams of the four possible cases. Namely, RL, LR, RR, and LL stand for  $(P_{e^+}, P_{e^-}) = (+1, -1), (-1, +1), (+1, +1), (-1, -1)$ , respectively. Figure 8 shows these spin configurations, the corresponding fractions (the fourth column), and the total spin projections onto the  $e^+e^-$  direction (the last column). This figure is adapted from Ref. [16].

Now, we give an expression of the left-right asymmetry  $A_{LR}$ , which has several advantages such as it being independent of detector efficiency asymmetries and its measurement having negligible systematic error. It is defined by

$$A_{LR} = \frac{\sigma(P_{e^+} = +1, P_{e^-} = -1) - \sigma(P_{e^+} = -1, P_{e^-} = +1)}{\sigma(P_{e^+} = +1, P_{e^-} = -1) + \sigma(P_{e^+} = -1, P_{e^-} = +1)}$$

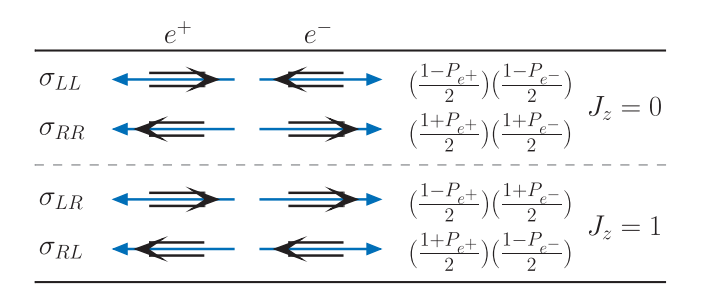


FIG. 8. The longitudinal spin configurations in electron-positron collisions. The thick arrow denotes the direction of motion of the particle, and the double arrow denotes its spin direction.

or equivalently

$$A_{LR} = \frac{\sigma_{RL} - \sigma_{LR}}{\sigma_{LR} + \sigma_{RL}} \tag{3.4}$$

for a given process. For the process  $e^+e^- \rightarrow ZZ$  considered in this study, it is obtained by

$$A_{LR}^{\text{Born}} = \frac{(c_L^e)^4 - (c_R^e)^4}{(c_L^e)^4 + (c_R^e)^4} = 0.40979$$
 (3.5)

at the Born level.

If  $e^+e^-$  is annihilated into a vector particle, only  $\sigma_{LR}$  and  $\sigma_{RL}$  (J=1 configurations) have a nonzero contribution. In this study, the  $\sigma_{LL}$  and  $\sigma_{RR}$  have the tiny values due to small electron mass effects, so they can be neglected. In this case, we can also rewrite the left-right asymmetry as [16]

$$A_{LR} = \frac{1}{P_{\text{eff}}} A_{LR}^{\text{obs}} = \frac{1}{P_{\text{eff}}} \left( \frac{\sigma_{-+} - \sigma_{+-}}{\sigma_{-+} + \sigma_{+-}} \right)$$
(3.6)

in terms of the effective polarization  $P_{\rm eff}$  and the measured left-right asymmetry  $A_{LR}^{\rm obs}$ ,

$$P_{\text{eff}} = \frac{(P_{e^{-}} - P_{e^{+}})}{(1 - P_{e^{-}} P_{e^{+}})}, \qquad A_{LR}^{\text{obs}} = \frac{\sigma_{-+} - \sigma_{+-}}{\sigma_{-+} + \sigma_{+-}}, \quad (3.7)$$

where the corresponding cross sections are given by

$$\sigma_{-+} = \frac{1}{4} [(1 + |P_{e^{+}}||P_{e^{-}}|)(\sigma_{RL} + \sigma_{LR}) + (|P_{e^{+}}| + |P_{e^{-}}|)(\sigma_{RL} - \sigma_{LR})]$$

$$\sigma_{+-} = \frac{1}{4} [(1 + |P_{e^{+}}||P_{e^{-}}|)(\sigma_{RL} + \sigma_{LR}) - (|P_{e^{+}}| + |P_{e^{-}}|)(\sigma_{RL} - \sigma_{LR})].$$
(3.8)

Another parameter, the effective luminosity  $\mathcal{L}_{\text{eff}}$  is given by

$$\frac{\mathcal{L}_{\text{eff}}}{\mathcal{L}} = \frac{1}{2} (1 - P_{e^{-}} P_{e^{+}}), \tag{3.9}$$

which basically reflects the fraction of particles that are interacting.

#### IV. PARAMETER SETTINGS

A set of input parameters must be specified with their corresponding numeric values, in order to provide consistent higher-order predictions in the SM. We set the input parameters as follows (see also Ref. [61]):

## (i) Mass parameters are

$$m_e = 0.510998928 \text{ MeV}, \qquad m_u = 73.56 \text{ MeV}, \ m_\mu = 105.6583715 \text{ MeV}, \qquad m_d = 73.56 \text{ MeV}, \ m_\tau = 1.77682 \text{ GeV}, \qquad m_s = 95 \text{ MeV}, \ M_W = 80.385 \text{ GeV}, \qquad m_c = 1.275 \text{ GeV}, \ M_Z = 91.1876 \text{ GeV}, \qquad m_b = 4.66 \text{ GeV}, \ M_h = 125 \text{ GeV}, \qquad m_t = 173.21 \text{ GeV}.$$

Here, the u- and d-quark masses are calculated as a effective parameters and are specially given for the  $M_Z$ -mass scale via the hadronic contributions

$$\Delta \alpha_{\text{had}}^{(5)}(M_Z) = \frac{\alpha}{\pi} \sum_{f=u,c,d,s,b} Q_f^2 \left( \ln \frac{M_Z^2}{m_f^2} - \frac{5}{3} \right)$$

$$\approx 0.027547. \tag{4.1}$$

According to Ref. [61], s-quark mass  $m_s$  is an estimate of a so-called current quark mass in the  $\overline{\rm MS}$  scheme at scale  $\mu\approx 2$  GeV.  $m_c\equiv m_c(m_c)$  is the "running" mass in the  $\overline{\rm MS}$  scheme, and  $m_b$  is the  $\Upsilon(1S)$  bottom quark mass.

(ii) The fine structure constant is

$$\alpha(0) = 1/137.03599907.$$
 (4.2)

(iii) The Fermi constant is

$$G_F = 1.1663787(6) \times 10^{-5} \text{ GeV}^{-2}, \quad (4.3)$$

which is conventionally defined via the muon lifetime

The renormalization scale  $\mu_R$  is fixed to center-of-mass energy,  $\sqrt{s}$ .

On the other hand, it is important to specify the electromagnetic coupling  $\alpha=e^2/(4\pi)$  for the EW  $\mathcal{O}(\alpha)$  corrections. For an obvious choice of  $\alpha$ , there are two different methods as follows: the fine-structure constant  $\alpha(0)$  in the Thompson limit  $[\alpha(0)$  scheme] and the running electromagnetic coupling  $\alpha(Q^2)$  at any energy scale Q. It is possible to use the value of  $\alpha(M_Z^2)\approx 1/129$   $[\alpha(M_Z^2)$  scheme], which is calculated by analyzing the experimental ratio  $R=\sigma(e^-e^+\to \mathrm{hadrons})/\sigma(e^-e^+\to \mu^-\mu^+)$  [62,63]. Another choice is a  $G_\mu$  scheme given by

$$\alpha(G_{\mu}) = \frac{\sqrt{2}G_{\mu}M_W^2}{\pi} \left(1 - \frac{M_W^2}{M_Z^2}\right). \tag{4.4}$$

An effective value of  $\alpha$  in this scheme is obtained as  $\alpha(G_{\mu}) \approx 1/132$  from the Fermi constant  $G_{\mu}$ .

The  $G_{\mu}$  scheme provides the possibility of absorbing some important universal corrections associated with the renormalization of the weak mixing angle into leading-order contributions. At next-to-leading order (NLO), the  $\alpha(0)$  and  $G_{\mu}$  schemes are related by

$$\alpha(G_u) = \alpha(0)[1 + \Delta r^{(1)}] + \mathcal{O}(\alpha^3),$$
 (4.5)

where  $\Delta r^{(1)}$  denotes the EW correction to muon decay at NLO [48,64]. In Sirlin's relation, the resummation is achieved by the replacement  $(1 + \Delta r^{(1)}) \rightarrow \frac{1}{(1 - \Delta r^{(1)})}$  in Eq. (4.5). One then obtains a much closer agreement between the two schemes. This fact also reveals that the  $G_{\mu}$  scheme provides more accurate results above the  $M_{Z}$ -mass scale unless one applies the leading-log resummation in the strict NLO  $\alpha$  scheme.

Actually, the suitability of the scheme directly relates to the nature of the considered process. In all cases, a common coupling factor  $\alpha^n$  should be used in full gauge-invariant subgroups; otherwise, significant consistency relations disappear [65].

In this study, we present the results obtained by both the  $\alpha(0)$  scheme and  $G_{\mu}$  scheme and discuss the difference due to these choices.

### V. NUMERICAL RESULTS AND DISCUSSIONS

We examine the Z-boson pair production in electron-positron collision, by taking into account a full one-loop EW  $\mathcal{O}(\alpha)$  corrections, including soft and hard QED radiation. We provide the center-of-mass energy dependence of Born and one-loop cross sections. To discuss the origin of the large correction, we also present the relative QED and weak corrections [as defined in Eq. (2.30)] as a function of the center-of-mass energy. We include the spin polarization effects of the initial electron and positron beams in the total cross sections. We discuss how the considered process is affected by beam polarization. The left-right asymmetry and angular distributions are also presented.

First of all, for the numerical verification of Born-level and hard photon bremsstrahlung calculations, we use three different tools FEYNARTS&FORMCALC, CALCHEP, and WHIZARD. In Table I, we give the results obtained by them for Born-level process  $e^-e^+ \rightarrow ZZ$  and hard process  $e^-e^+ \rightarrow ZZ\gamma$  at  $\sqrt{s}=250$ , 500, and 1000 GeV. It is found that Born-level results are an excellent agreement. The hard photon bremsstrahlung results are in good agreement up to five digits.

In Fig. 9, we plot the Born and one-loop cross sections and the relative corrections as a function of center-of-mass

TABLE I. The Born and hard photon bremsstrahlung cross sections obtained by FEYNARTS&FORMCALC (FA&FC), WHIZARD, and CALCHEP.

$\sqrt{s}$	250 GeV	500 GeV	1000 GeV
	$\sigma^{ m Bo}$	$rm(e^-e^+ \rightarrow Z^0Z^0)$	(fb)
FA&FC	991.500(2)	315.463(9)	79.592(8)
WHIZARD	991.501(5)	315.464(3)	79.595(1)
CALCHEP	991.50	315.46	79.593
	$\sigma^{ m hard}$	$e^{-\gamma}(e^-e^+  o Z^0Z^0\gamma)$	(fb)
FA&FC	144.443(4)	52.751(9)	14.852(4)
WHIZARD	144.457(1)	52.739(5)	14.851(3)
CALCHEP	144.46	52.758	14.859

energy. We also show the proposed energies of future colliders with the vertical solid lines. The center-of-mass energy ranges from 190 GeV to 1.5 TeV in steps of 10 GeV. Since the colliding energy  $\sqrt{s}$  starts near the threshold of  $2m_Z$ , the Born and one-loop cross sections increase quickly with the opening of the phase space, reach a maximum value, and then fall off rapidly with the increment of  $\sqrt{s}$ . This is also the expected behavior. The one-loop cross section reaches a maximum of 1109.93 fm with  $\delta_{\text{Total}} = -8.45\%$  at  $\sqrt{s} = 210$  GeV and then decreases to 40.04 fb with  $\delta_{\text{Total}} = +14.17\%$  at  $\sqrt{s} = 1.5$  TeV. The pure QED corrections make a positive contribution and increase from -8.1% to +31.15% when  $\sqrt{s}$  goes from 200 GeV to 1.0 TeV. On the other hand, the weak corrections make a negative contribution, and its relative correction decreases

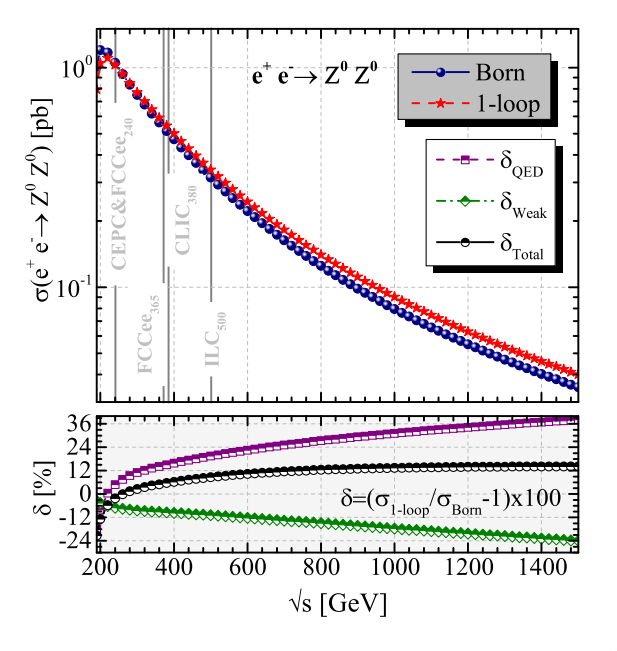


FIG. 9. Born and one-loop cross sections as a function of  $\sqrt{s}$ . The relative corrections in a percentage is also shown at the bottom panel. The vertical solid lines show the proposed energies for various future colliders.

from -4.63% to -17.69%. The QED and weak corrections partially compensate each other, providing relative corrections of around -12.73% at the first point and +13.46% at 1.0 TeV. The EW radiative corrections significantly increase with the  $\sqrt{s}$ . This is due to the presence already at the one-loop order, of large double and single logarithm terms behaving like  $(\alpha/\pi) \ln^2 s$  and  $(\alpha/\pi) \ln s$ .

These results show that the pure QED and weak corrections are the same order of magnitude, so that both are equally important. However, the QED correction makes the main contribution to the total EW correction. The relative radiative correction due to full EW one-loop contributions in the vicinity  $\sqrt{s}$  close to the threshold of production ZZ becomes rather large. This effect is due to the Coulomb singularity in Feynman diagrams, which includes the instantaneous virtual photon exchange in the loop that has a small spatial momentum. Overall, the full EW one-loop corrections enhance the Born cross section. While the energy-dependent structure of both the OED and weak corrections is clearly visible, it almost disappears in the total corrections at higher energies. For proposed colliding energies of the future collider projects, CEPC (at  $\sqrt{s} = 240 \text{ GeV}$ ), FCCee (at  $\sqrt{s} = 350 \text{ GeV}$ ), CLIC (at  $\sqrt{s} = 380 \text{ GeV}$ ), and ILC (at  $\sqrt{s} = 500 \text{ GeV}$ ), the unpolarized born-level cross sections reach 1051.44 (with  $\delta_{\text{Total}} = -2.20\%$ ), 588.23 (with  $\delta_{\text{Total}} = +4.73\%$ ), 513.82 (with  $\delta_{\text{Total}} = +5.70\%$ ), and 315.46 fb (with  $\delta_{\text{Total}} = +8.66\%$ ), respectively. The production rate of  $e^-e^+ \rightarrow ZZ$  is larger by around 1 order of magnitude than from the  $\gamma\gamma$ -collision mode (see Refs. [66,67]).

In Fig. 10, we plot the virtual, soft, and hard photonic corrections as a function of  $\sqrt{s}$ . The virtual corrections decrease from 0.24 to -0.06, while the soft bremsstrahlung corrections remain nearly constant with a value of -0.91 with the increment of  $\sqrt{s}$ . However, hard bremsstrahlung corrections, i.e., collinear and noncollinear parts, start from

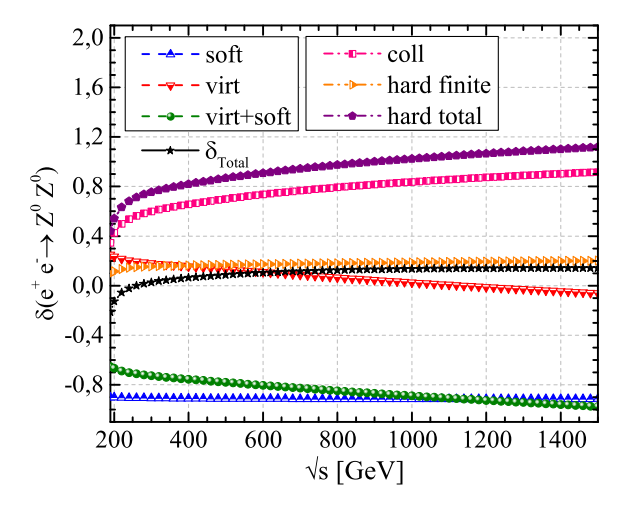


FIG. 10. The effect of different individual contributions on cross sections as a function of  $\sqrt{s}$ .

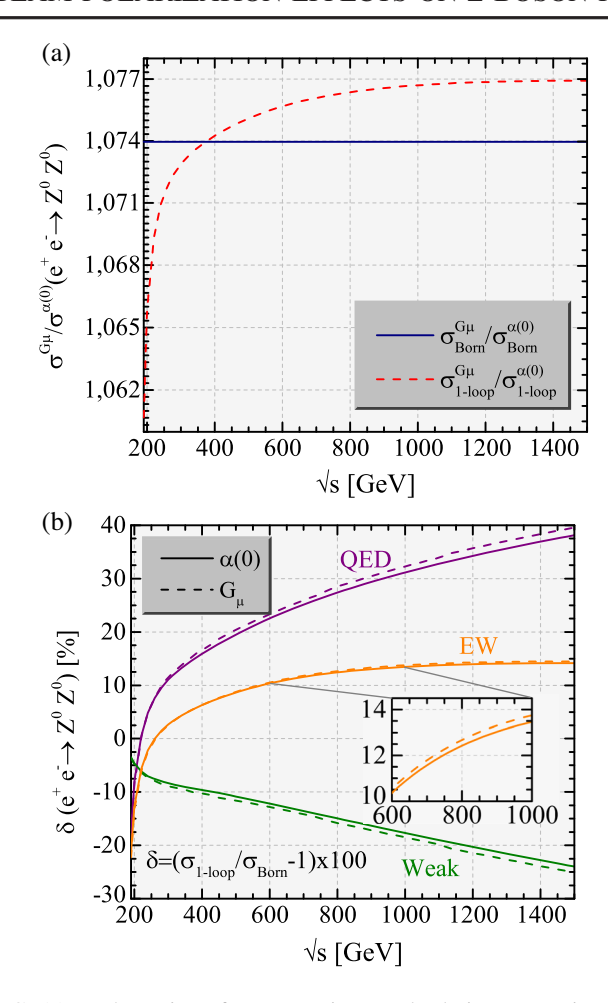


FIG. 11. The ratios of cross sections and relative corrections in two different schemes,  $\alpha(0)$  and  $G_{\mu}$  schemes, as a function of  $\sqrt{s}$ .

their minimum values and then increase rapidly with the increment of  $\sqrt{s}$ . Consequently, the virt + soft and hard bremsstrahlung corrections are partially canceled, as they are combined into the full EW corrections. The soft and hard bremsstrahlung corrections make the negative and positive dominant contributions to the full EW corrections, respectively.

For  $\alpha(0)$  and  $G_{\mu}$  schemes, we present the ratios of cross sections in Fig. 11(a) and the relative corrections in Fig. 11(b) as a function of  $\sqrt{s}$ , respectively. In Table II, we also provide our numerical results obtained in the  $\alpha(0)$  and  $G_{\mu}$  schemes for  $\sqrt{s}=250$ , 500, and 1000 GeV. The Born cross section increase by about 7.39% in the  $G_{\mu}$  scheme as compared to the  $\alpha(0)$  scheme. When  $\sqrt{s}$  goes up from 200 GeV to 1.5 TeV, the one-loop cross section in the  $G_{\mu}$  scheme is from 6.58% to 7.69% larger than ones in the  $\alpha(0)$  scheme. The QED relative corrections in the  $G_{\mu}$  scheme increase by up to about 4%, while the weak relative corrections decrease by up to about 5%, as compared to the  $\alpha(0)$  scheme. However, the difference between total relative corrections in considered schemes is 1%, so small that it can be considered as a theoretical uncertainty.

TABLE II. Born and one-loop cross sections and relative corrections of  $e^+e^- \to Z^0Z^0$  in the  $\alpha(0)$  scheme and  $G_\mu$  scheme for various values of  $\sqrt{s}$ .

$\sqrt{s}$	250 GeV	500 GeV	1000 GeV	
		$\sigma(e^+e^- \to Z^0Z^0)$ (fb)		
$\sigma_{ m Born}^{lpha(0)}$	991.50	315.46	79.59	
$\sigma_{ m Born}^{G_{\mu}}$	1064.83	338.88	85.48	
$\sigma_{\text{1-loop}}^{\alpha(0)}$	981.59	342.77	90.31	
$\sigma_{ ext{1-loop}}^{G_{\mu}}$	1051.67	368.51	97.24	
		$\delta(e^+e^- \to Z^0Z^0) \ (\%)$		
$\delta_{ ext{QED}}^{a(0)}$	+6.35	+19.50	+31.15	
$\delta_{ ext{QED}}^{G_{\mu}}$	+6.39	+20.38	+32.27	
$\delta_{ m Weak}^{lpha(0)}$	-7.35	-10.85	-17.69	
$\delta_{ m Weak}^{G_{\mu}}$	-7.63	-11.61	-18.52	
$\delta^{lpha(0)}_{ ext{Total}}$	-1.00	+8.65	+13.46	
$\delta_{ ext{Total}}^{G_{\mu}}$	-1.24	+8.77	+13.75	

Now, we examine the initial beam polarization dependence of the Born and the one-loop cross sections ( $\sigma_{\mathrm{Born}}^{\overrightarrow{P}_{e^+}P_{e^-}}$ and  $\sigma_{1\text{-loop}}^{P_{e^+}P_{e^-}}$ ) on  $\sqrt{s}$ . Also, we present the total relative corrections in order to see effect of polarization configurations on the EW corrections. Figure 12(a) shows unpolarized and completely polarized initial beams cases. Here, we use the following notation:  $\sigma^{RL}$  denotes the total cross section with the 100% right-handed polarized positron  $(P_{e^+} = +1)$  and the 100% left-handed polarized electron  $(P_{e^-}=-1)$  beams,  $(e_R^+,e_L^-)$ . Others can be defined analogously. We note that  $\sigma^{LL}$  and  $\sigma^{RR}$  are very small  $[\mathcal{O}(10^{-10})]$ pb] as expected and are thus not included here. All curves for polarized and unpolarized cases increase quickly with the opening of the phase space, reach a maximum value, and then fall off rapidly with the increment of  $\sqrt{s}$ . Their maximum values are reached at around  $\sqrt{s} \sim 210$  GeV. The one-loop polarized cross sections  $\sigma_{\text{1-loop}}^{\text{LR}}$  and  $\sigma_{\text{1-loop}}^{\text{RL}}$  can be enhanced by about factors of 1.5 and 2.5, respectively, compared with the unpolarized case. For instance, at  $\sqrt{s} = 250$  GeV,  $\sigma_{\rm Born}^{\rm RL}$  reaches a value of 2.80 pb, yielding a total relative correction of about -10.71%. At  $\sqrt{s}=250$  GeV,  $\sigma_{\mathrm{Born}}^{\mathrm{LR}}$  reaches a value of 1.17 pb, yielding a total relative correction of +22.20%. While  $\sigma_{\rm Born}^{\rm RL}$  is around two times larger than  $\sigma_{Born}^{RL}$ , the relative corrections of the former are smaller than that of the latter. Namely,  $(e_L^+e_R^-)$  polarization case has larger EW radiative corrections than other cases.

Figure 12(b) shows the results for various polarization degrees of the initial beams,  $(P_{e^+}, P_{e^-}) = (0.0, -0.8)$ , (+0.3, -0.8), (+0.6, -0.8), proposed by the future colliders. The cross sections at both Born and one-loop levels are sorted according to various polarization degrees of

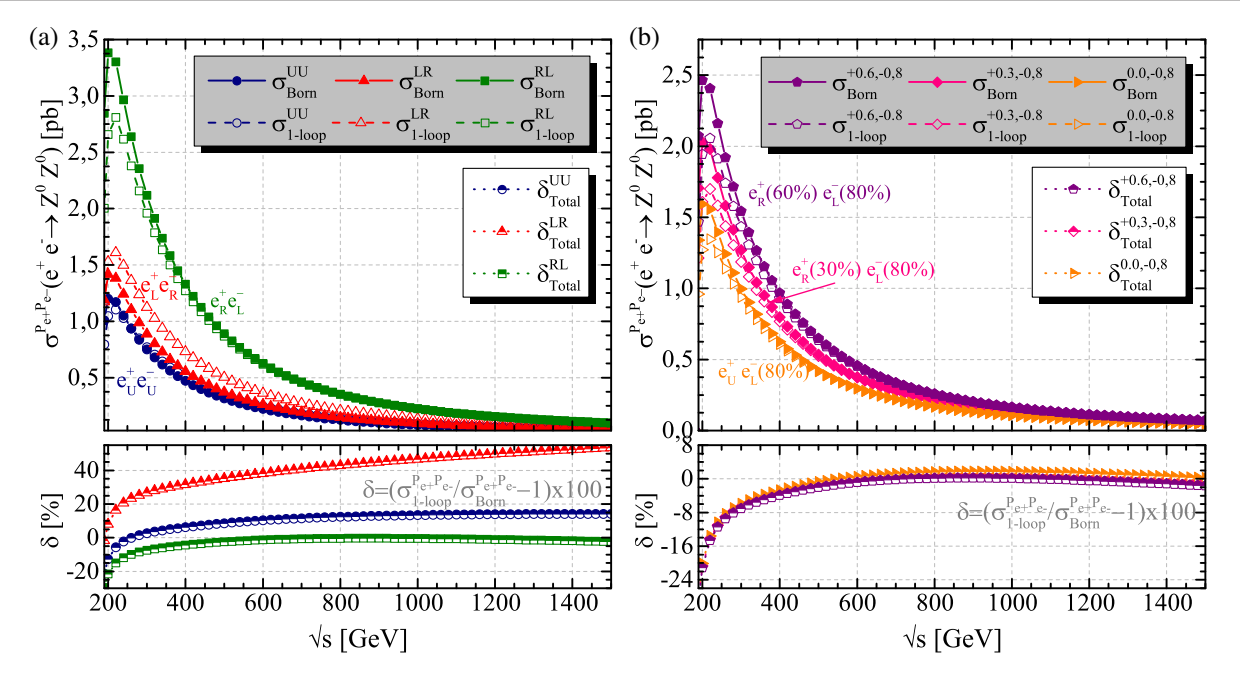


FIG. 12. Polarized Born and one-loop cross sections as a function of  $\sqrt{s}$ .

initial beams as follows:  $\sigma^{\rm RL} > \sigma^{+0.6,-0.8} > \sigma^{+0.3,-0.8} > \sigma^{0.0,-0.8} > \sigma^{\rm LR} > \sigma^{\rm UU}$ . There appears a similar energy dependence behavior in polarized cases as in the unpolarized case. The one-loop cross section with the polarization degrees of  $(P_{e^+}, P_{e^-}) = (+0.6, -0.8)$ , i.e.,  $\sigma^{(+0.6, -0.8)}_{1\text{-loop}}$ , has a maximum of 2.05 pb, providing a total relative correction of -14.59%. When  $\sqrt{s}$  goes from 240 GeV to 1.0 TeV, the relative corrections vary from about -11% to +1.69%, +0.75%, and +0.14% for  $(P_{e^+}, P_{e^-}) = (0.0, -0.8), (+0.3, -0.8), (+0.6, -0.8)$ , respectively. We obtain the following results for proposed polarization cases by the future collider projects:  $\sigma^{+0.3,-0.8}_{1\text{-loop}} = 1.51$  pb with

 $\delta_{\text{Total}}^{+0.3,-0.8} = -9.90\%$  at  $\sqrt{s} = 250$  GeV (ILC) and  $\sigma_{\text{1-loop}}^{0,-0.8} = 0.66$  pb with  $\delta_{\text{Total}}^{0,-0.8} = -3.94\%$  at  $\sqrt{s} = 380$  GeV (CLIC). In Figs. 13 and 14, the Born cross section and the total relative correction are also presented in the plane of polarization degrees of the incoming beams  $(P_{e^+}, P_{e^-})$  for  $\sqrt{s} = 250$  GeV and  $\sqrt{s} = 500$  GeV, respectively. The  $P_{e^+}$  and  $P_{e^-}$  range from -1 to +1. We also show some values by the contour lines. The beam polarization dependence of the relative correction is calculated from  $\delta_{\text{Total}}^{P_{e^+}P_{e^-}} = (\sigma_{1\text{-loop}}^{P_{e^+}P_{e^-}} / \sigma_{\text{Born}}^{P_{e^+}P_{e^-}} - 1)$  by using Eq. (3.3). The Born cross section reaches its larger values at the left top corner

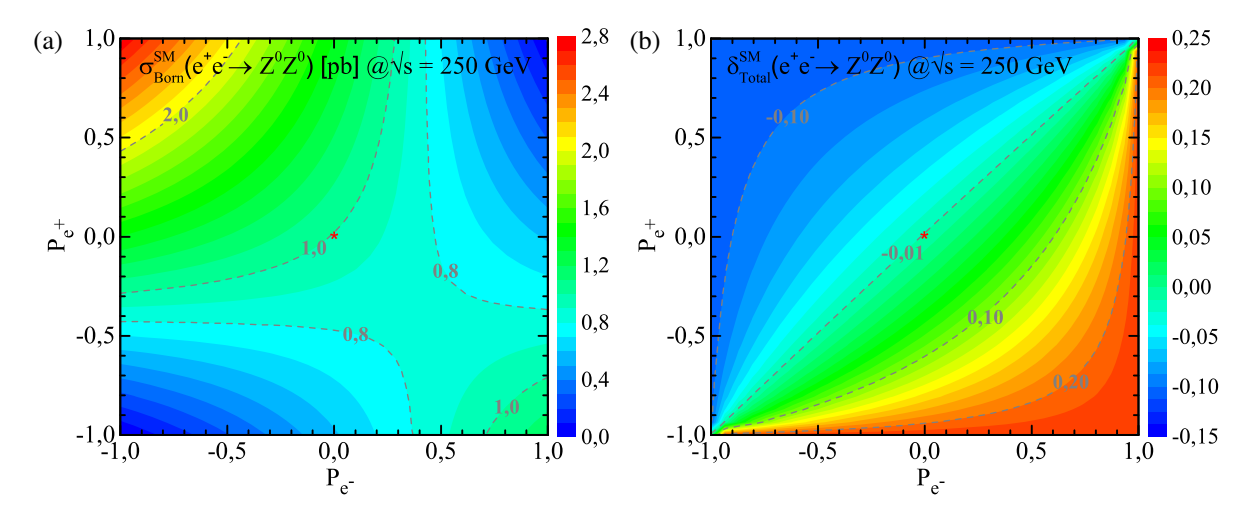


FIG. 13. Beam polarization effects on the Born cross section and on the total relative correction for  $\sqrt{s} = 250$  GeV. The color heat maps correspond to the values of born cross section (left plot) and the total EW relative correction (right plot). The asterisk denotes the unpolarized point  $(P_{e^+}, P_{e^-}) = (0, 0)$ .

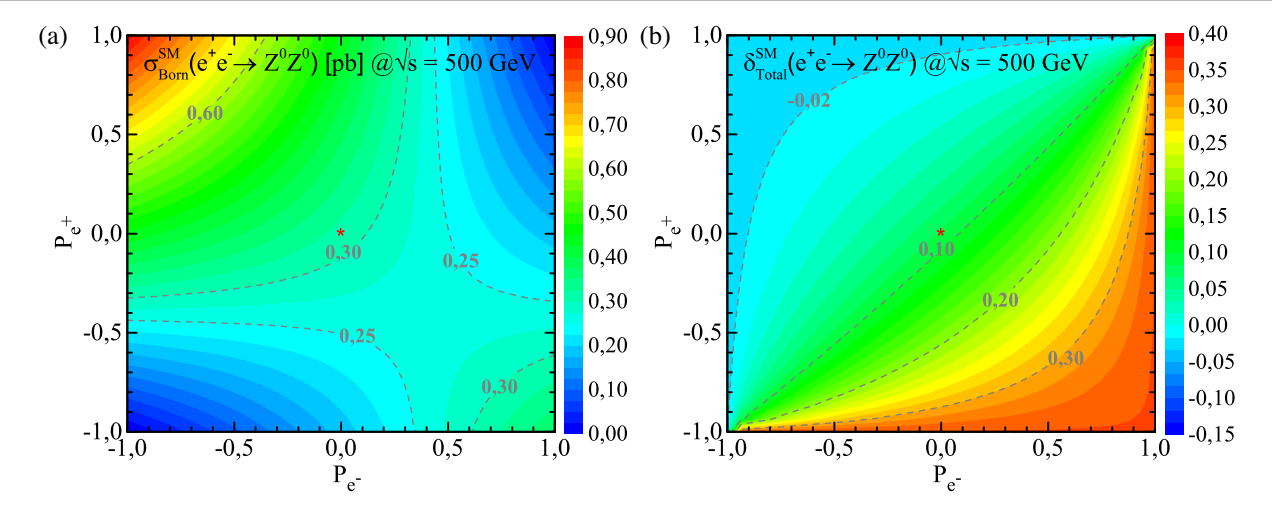


FIG. 14. Same as in Fig. 13 but for  $\sqrt{s} = 500$  GeV.

 $(0 < P_{e^+} \le +1 \text{ and } -1 \le P_{e^-} < 0)$ , whereas it has smaller values at the right top and left bottom corners. As expected, it has a maximum value at point  $(P_{e^+}, P_{e^-}) = (+1, -1)$ , namely, 100% left-handed polarized electron and 100% right-handed polarized positron. The total relative correction reaches positive and larger values at the right bottom corner  $(-1 \le P_{e^+} < 0 \text{ and } 0 < P_{e^-} \le +1)$ . As the values of polarization degrees approach  $P_{e^-} \to +1$  and  $P_{e^+} \to -1$ , the relative correction increases. Particularly, significant positive corrections are observed in the region below the 0.10 contour line. Together with the larger cross sections, smaller systematic errors can be expected for the cross section measurement with the polarized beams than in the unpolarized case.

A convenient observable is the left-right asymmetry when applying polarized beams. This asymmetry is especially important for high-precision measurements. Therefore, we present the left-right asymmetry of the cross sections, which is defined in Eq. (3.4), as a function of center-of-mass energy in Fig. 15. For Born level, the left-right asymmetry remains

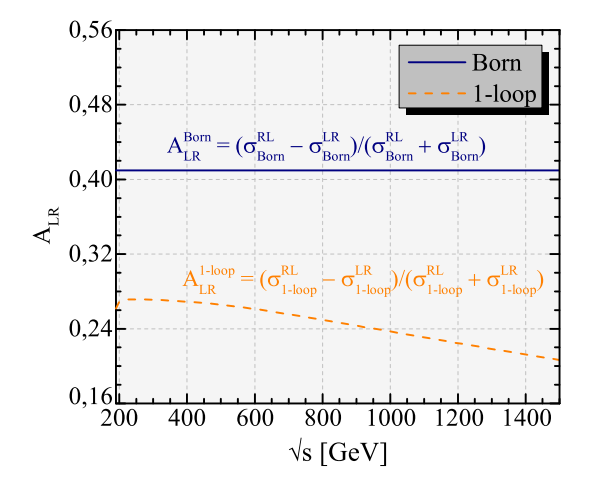


FIG. 15. The left-right asymmetry as a function of  $\sqrt{s}$ .

constant at 0.40979 with the increment of  $\sqrt{s}$ . This value is exactly the same as the result calculated theoretically in Eq. (3.5). On the other hand, at one-loop level, the left-right asymmetry decreases from 0.2616 to 0.2065, as the

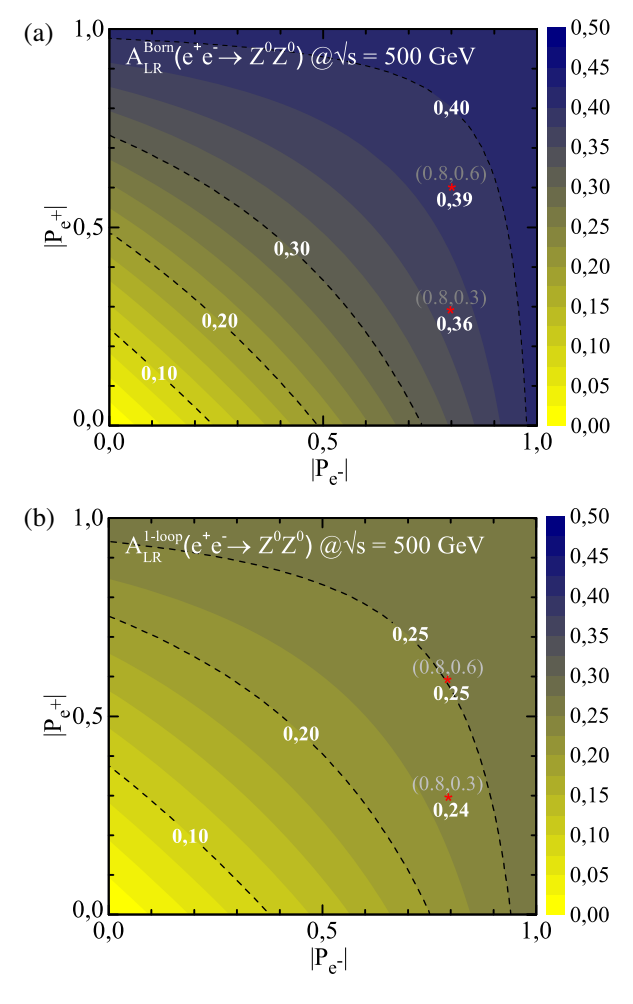


FIG. 16. The left-right asymmetry in the plane of polarization degrees of the incoming beams  $(P_{e^+}, P_{e^-})$  for  $\sqrt{s} = 500$ .

TABLE III. Born and one-loop cross sections, relative correction, and left-right asymmetry for various polarization configurations at  $\sqrt{s} = 250$ . Here, we define the scaling factor as  $R_X^{P_e+P_e-} = \sigma_X^{P_e+P_e-}/\sigma_X^{0,0}$ , where X stands for Born or one-loop level.

$(P_{e^+},P_{e^-})$	$P_{ m eff}$	$L_{ m eff}/L$	$A_{LR}^{\mathrm{obs}}(\mathrm{Born})$	$A_{LR}^{\text{obs}}(1\text{-loop})$	$\sigma_{\rm Born}$ (fb)	$\sigma_{1\text{-loop}}$ (fb)	$\delta_{ ext{Total}}(\%)$	$R_{Born}^{P_{e^+}P_{e^-}}$	$R^{P_{e^+}P_{e^-}}_{\text{1-loop}}$
(0, 0)	0	0.50	0	0	991.50	981.59	-0.99%	1.00	1.00
(+1.0, -1.0)	-1.00	1.00	0.4098	0.2715	2795.61	2496.35	-10.71%	2.82	2.54
(-1.0, +1.0)	+1.00	1.00	0.4098	0.2715	1170.39	1430.25	+22.20%	1.18	1.46
(0.0, -1.0)	-1.00	0.50	0.4098	0.2715	1397.81	1248.17	-10.70%	1.41	1.27
(0.0, -0.8)	-0.80	0.50	0.3278	0.2172	1316.54	1194.87	-9.24%	1.33	1.22
(0.0, +0.8)	+0.80	0.50	0.3278	0.2172	666.46	768.43	+15.30%	0.67	0.78
(+0.3, -0.8)	-0.89	0.62	0.3635	0.2409	1676.40	1510.42	-9.90%	1.69	1.54
(-0.3, +0.8)	+0.89	0.62	0.3635	0.2409	782.52	924.07	+18.09%	0.79	0.94
(+0.6, -0.8)	-0.95	0.74	0.3876	0.2568	2036.25	1825.98	-10.33%	2.05	1.86
(-0.6, +0.8)	+0.95	0.74	0.3876	0.2568	898.59	1079.71	+20.16%	0.91	1.10

center-of-mass energy goes up from 190 to 1500 GeV. Consequently, the radiative corrections can conveniently be described by the one-loop induced deviation from its value at Born level.

In Figs. 16(a) and 16(b), we plot the left-right asymmetry of the cross sections  $A_{LR}^{\rm obs}$ , which is defined in Eq. (3.6), as a function of polarization degrees of  $(P_{e^+}, P_{e^-})$ . Some values are also shown with contour lines. We note that the results are symmetric with respect to the exchange of  $P_{e^+} \leftrightarrow P_{e^-}$ , since they only appear by their absolute values in the Eq. (3.8). It is obvious that the left-right asymmetry  $A_{LR}^{\rm obs}$  increases as both  $|P_{e^+}|$  and  $|P_{e^-}|$  run from 0 to 1. The maximum values are reached at the point  $(|P_{e^+}|, |P_{e^-}|) = (1, 1)$ . These values are 0.40979 and 0.2657 for Born and one-loop levels, respectively. In these figures, we also mark some special points by an asterisk.

Table III presents the numerical values of the polarized cross sections, the relative corrections, and the left-right asymmetry  $A_{LR}^{\rm obs}$  for various polarization degrees of the

initial beams. The values of effective polarization and effective luminosity, which are calculated by Eqs. (3.7) and (3.9), respectively, are also given. It is clear that the production rate can be enhanced if  $P_{e^-}$  and  $P_{e^+}$  have negative and positive signs, respectively. In particular, the longitudinally  $(P_{e^+}, P_{e^-}) = (+1, -1)$  polarizations of the initial beams significantly improve the cross section.

Figures 17(a) and 17(b) show the differential cross sections at Born and one-loop levels as a function of the angle between the coming electron and the outgoing Z boson for  $\sqrt{s} = 250$  and 500 GeV, respectively. The angular dependence of the QED, weak, and total EW relative corrections is also shown in the same figures. For Born and one-loop cross sections, the angular distribution peaks significantly in the (symmetrically) forward and backward directions. The relative corrections modify somewhat the Born angular distribution because their influence is larger in the central region. The total corrections reach their maximum values, when  $\cos\theta$  goes to the extreme points

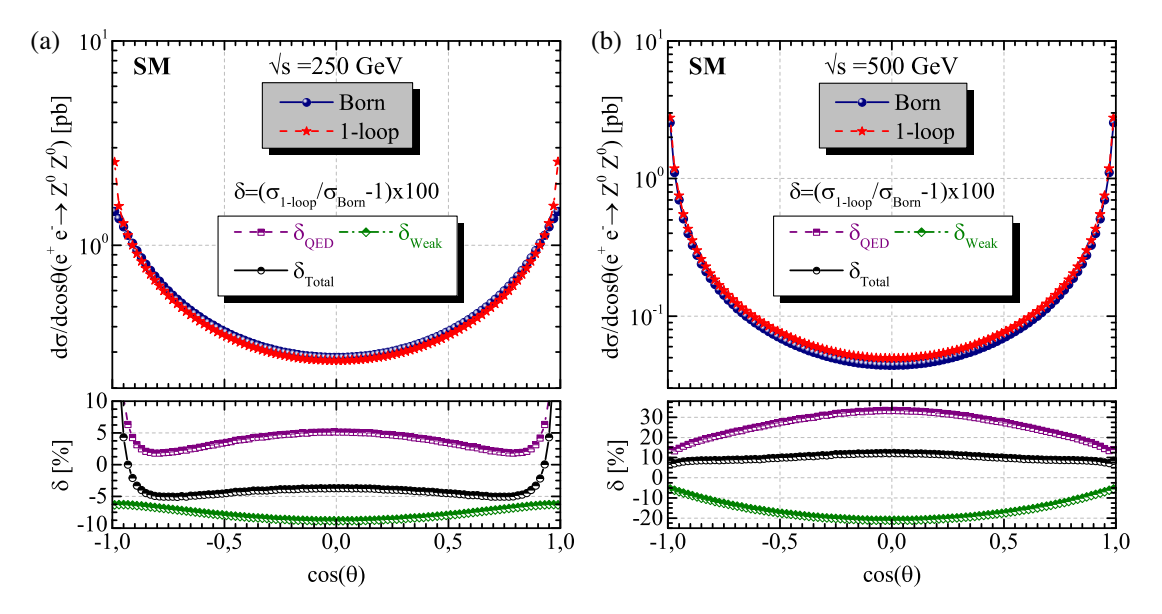


FIG. 17. Born and one-loop angular distributions for (a)  $\sqrt{s} = 250$  GeV and (b)  $\sqrt{s} = 500$  GeV.

-1 or +1 for  $\sqrt{s} = 250$  and zero point for  $\sqrt{s} = 500$ . Namely, the Z bosons are dominantly produced in the forward and backward directions for  $\sqrt{s} = 250$ , whereas they are produced in the central region for  $\sqrt{s} = 500$ . Therefore, it will be more likely to observe them in these collision regions. For all values of  $\cos \theta$ , the QED corrections make positive contributions, while the weak corrections supply negative contributions. The same behavior is observed as in the total cross sections. The QED and weak contributions are partially offset by each other into EW contributions. While both corrections show a significant dependence on  $\cos \theta$  separately, this decreases for full EW corrections. When  $\cos \theta$  runs from 0 to +0.95 or -0.95, at  $\sqrt{s} = 250$  GeV, the total relative correction  $\delta_{\text{Total}}$  increases from -3.71% to 4.30%, while it decreases 12.2% to 7.7%at  $\sqrt{s} = 500$  GeV.

### VI. SUMMARY AND CONCLUSIONS

For further sensitivity testing of the SM, as well as to look for clues on the BSM, high-precision calculations should be performed. At least, a full set of one-loop corrections in the production channels must be included to ensure adequate accuracy. However, the extent to which higher-order computations beyond one-loop order will be needed depends largely on the expected experimental accuracy.

In this work, by considering a full set of one-loop EW corrections, we have investigated the Z-boson pair production at electron-positron collisions. The UV divergences have been organized by dimensional regularization on the OS scheme. Furthermore, the IR divergences have been removed by the inclusion of the soft and hard bremsstrahlung corrections. Also, the collinear divergences have been corrected by the phase-space slicing method. We have verified the stability of our results against the angular and soft cutoff parameters  $\Delta_c$ ,  $\Delta_s$ , as well as the IR regulator  $m_\gamma$ . We have also compared the results from WHIZARD and CALCHEP for the Born and hard photon bremsstrahlung cross sections with the results of the packages used in this work and obtained very good agreement (up to six digits).

We have carried out the numerical evaluation for the  $\alpha(0)$  and  $G_{\mu}$  schemes. The differences between these schemes for the QED and weak relative corrections are about 4% and 5%, respectively, whereas this is 1% for the total

relative correction. This can be considered as a theoretical uncertainty.

Our results show that the Born cross section is commonly increased by the one-loop EW radiative corrections and the total relative correction is typically up to about 10%. The pure QED and weak corrections are the same order of magnitude, so both are important for precision calculation. The QED and weak contributions are partially offset by each other into EW contributions. However, the QED correction makes the main contribution to the total EW correction.

Moreover, we have investigated the spin polarization effects of the initial beams on the total cross sections. We have observed that the radiative corrections have a large polarization dependence. As a result, an improvement has been observed by a factor of 2.5 with the 100% right-handed polarized positron and the 100% left-handed polarized electron beams, compared with the unpolarized case. The left-right asymmetry and angular distributions have also presented. The Born and one-loop angular distributions are symmetric and strongly peaked in the forward and backward directions. For all angles, the QED corrections make positive contributions, while the weak corrections supply negative contributions. The relative corrections slightly change the Born angular distribution, as their effect is usually larger in the central region.

In summary, an analysis of the one-loop EW radiative corrections to Z-boson pair production in electron-positron collisions has been carried out in the framework of the SM. The initial beam effects on the cross sections have been discussed in detail. It has been clearly shown that one-loop EW radiative corrections significantly alter the lowest-order results and should therefore be fully accounted for a realistic description of experiments at future collider energies. Our results provide precise predictions for Z-boson pair production, which can be tested as experiments achieve higher accuracy.

#### ACKNOWLEDGMENTS

The work of M. D. was supported by the Scientific and Technological Research Council of Turkey (TUBITAK) in the framework of 2219-International Postdoctoral Research Fellowship Program. This work was also supported in part by the National Science Foundation Grant No. PHY-2108339.

<sup>[1]</sup> S. L. Glashow, Nucl. Phys. 22, 579 (1961).

<sup>[2]</sup> S. Weinberg, Phys. Rev. Lett. 19, 1264 (1967).

<sup>[3]</sup> A. Salam, Conf. Proc. C 680519, 367 (1968).

<sup>[4]</sup> G. Aad et al. (ATLAS Collaboration), Phys. Lett. B 716, 1 (2012).

<sup>[5]</sup> S. Chatrchyan *et al.* (CMS Collaboration), Phys. Lett. B **716**, 30 (2012).

<sup>[6]</sup> G. Aad *et al.* (ATLAS and CMS Collaborations), J. High Energy Phys. 08 (2016) 045.

<sup>[7]</sup> P. Bambade et al., arXiv:1903.01629.

- [8] H. Baer et al., arXiv:1306.6352.
- [9] H. Aihara et al., arXiv:1901.09829.
- [10] E. Accomando *et al.* (CLIC Physics Working Group), arXiv: hep-ph/0412251.
- [11] The CEPC Study Group, arXiv:1811.10545.
- [12] M. Benedikt *et al.*, Report No. CERN-ACC-2019-0007, CERN, 2019.
- [13] A. Abada et al. Eur. Phys. J. Special Topics 228, 261 (2019).
- [14] A. A. Pankov, A. V. Tsytrinov, and N. Paver, Phys. Rev. D 73, 115005 (2006).
- [15] P. Osland, A. A. Pankov, and A. V. Tsytrinov, Eur. Phys. J. C 67, 191 (2010).
- [16] G. Moortgat-Pick et al., Phys. Rep. 460, 131 (2008).
- [17] R. W. Brown and K. O. Mikaelian, Phys. Rev. D 19, 922 (1979).
- [18] K. J. F. Gaemers and G. J. Gounaris, Z. Phys. C 1, 259 (1979).
- [19] A. Denner and T. Sack, Nucl. Phys. B306, 221 (1988).
- [20] G. J. Gounaris, J. Layssac, and F. M. Renard, Phys. Rev. D 67, 013012 (2003).
- [21] G. Abbiendi *et al.* (OPAL Collaboration), Phys. Lett. B 476, 256 (2000).
- [22] LEP, ALEPH, DELPHI, L3, OPAL, LEP Electroweak Working Group, SLD Electroweak Group, SLD Heavy Flavor Group Collaborations, arXiv:hep-ex/0312023.
- [23] P. Achard *et al.* (L3 Collaboration), Phys. Lett. B **572**, 133 (2003).
- [24] S. Jadach, W. Płaczek, and B. F. L. Ward, Phys. Rev. D 56, 6939 (1997).
- [25] G. J. Gounaris, J. Layssac, and F. M. Renard, Phys. Rev. D 61, 073013 (2000).
- [26] R. Rahaman and R. K. Singh, Eur. Phys. J. C 77, 521 (2017).
- [27] S. C. İnan and A. V. Kisselev, J. High Energy Phys. 10 (2021) 121.
- [28] S. Spor, E. Gurkanli, and M. Köksal, Nucl. Phys. B979, 115785 (2022).
- [29] J. Alcaraz, M. A. Falagán, and E. Sánchez, Phys. Rev. D 61, 075006 (2000).
- [30] G. J. Gounaris, J. Layssac, and F. M. Renard, Phys. Rev. D 62, 073013 (2000).
- [31] G. Aad *et al.* (ATLAS Collaboration), J. High Energy Phys. 03 (2013) 128.
- [32] M. Demirci and A. I. Ahmadov, Phys. Rev. D 94, 075025 (2016).
- [33] M. Demirci, Phys. Rev. D 100, 075006 (2019).
- [34] M. Demirci, Nucl. Phys. B961, 115235 (2020).
- [35] M. Demirci and M. F. Mustamin, Phys. Rev. D **103**, 113004 (2021).
- [36] J. J. Su, W. G. Ma, R. Y. Zhang, S. M. Wang, and L. Guo, Phys. Rev. D 78, 016007 (2008).

- [37] F. Boudjema, Le D. Ninh, S. Hao, and M. M. Weber, Phys. Rev. D 81, 073007 (2010).
- [38] S. Heinemeyer and C. Schappacher, Eur. Phys. J. C 76, 220 (2016).
- [39] S. Heinemeyer and C. Schappacher, Eur. Phys. J. C 78, 536 (2018).
- [40] L. He-Yi, Z. Ren-You, Ma Wen-Gan, J. Yi, and L. Xiao-Zhou, Chin. Phys. C 46, 043105 (2022).
- [41] J. Küblbeck, M. Böhm, and A. Denner, Comput. Phys. Commun. **60**, 165 (1990).
- [42] T. Hahn, Comput. Phys. Commun. 140, 418 (2001).
- [43] T. Hahn and M. Perez-Victoria, Comput. Phys. Commun. **118**, 153 (1999).
- [44] T. Hahn, Comput. Phys. Commun. 168, 78 (2005).
- [45] W. Kilian, T. Ohl, and J. Reuter, Eur. Phys. J. C 71, 1742 (2011).
- [46] M. Moretti, T. Ohl, and J. Reuter, arXiv:hep-ph/0102195.
- [47] A. Belyaev, N. D. Christensen, and A. Pukhov, Comput. Phys. Commun. **184**, 1729 (2013).
- [48] A. Denner, Fortschr. Phys. 41, 307 (1993).
- [49] G. 't Hooft and M. Veltman, Nucl. Phys. B44, 189 (1972).
- [50] T. Kinoshita, J. Math. Phys. (N.Y.) 3, 650 (1962).
- [51] T.D. Lee and M. Nauenberg, Phys. Rev. **133**, B1549 (1964).
- [52] J. Schwinger, Phys. Rev. 76, 790 (1949).
- [53] K. Fabricius, G. Kramer, G. Schierholz, and I. Schmitt, Z. Phys. C 11, 315 (1982).
- [54] G. Kramer and B. Lampe, Fortschr. Phys. 37, 161 (1989).
- [55] H. Baer, J. Ohnemus, and J. F. Owens, Phys. Rev. D 40, 2844 (1989).
- [56] B. W. Harris and J. F. Owens, Phys. Rev. D 65, 094032 (2002).
- [57] G. 't Hooft and M. Veltman, Nucl. Phys. **B153**, 365 (1979).
- [58] U. Baur, S. Keller, and D. Wackeroth, Phys. Rev. D **59**, 013002 (1998).
- [59] T. Omori, Report No. KEK-PREPRINT-98-237, KEK,
- [60] K. I. Hikasa, Phys. Rev. D 33, 3203 (1986).
- [61] P. A. Zyla et al. (Particle Data Group), Prog. Theor. Exp. Phys. 2020, 083C01 (2020).
- [62] H. Burkhardt and B. Pietrzyk, Phys. Lett. B 356, 398 (1995).
- [63] S. Eidelman and F. Jegerlehner, Z. Phys. C 67, 585 (1995).
- [64] A. Sirlin, Phys. Rev. D 22, 971 (1980).
- [65] A. Denner and S. Dittmaier, Phys. Rep. 864, 1 (2020).
- [66] G. J. Gounaris, J. Layssac, P. I. Porfyriadis, and F. M. Renard, Eur. Phys. J. C 13, 79 (2000).
- [67] D. Bardin, S. Bondarenko, P. Christova, L. Kalinovskaya, W. von Schlippe, and E. Uglov, Phys. Part. Nucl. Lett. 14, 811 (2017).